V^0 production in p+A collisions at $\sqrt{s} = 41.6\,\text{GeV}$

The HERA-B Collaboration

I. Abt[24], M. Adams[11], M. Agari[14], H. Albrecht[13], A. Aleksandrov[30], V. Amaral[9], A. Amorim[9], S. J. Aplin[13], V. Aushev[17], Y. Bagaturia[13,37], V. Balagura[23], M. Bargiotti[6], O. Barsukova[12], J. Bastos[9], J. Batista[9], C. Bauer[14], Th. S. Bauer[1], A. Belkov[12,†], Ar. Belkov[12], I. Belotelov[12], A. Bertin[6], B. Bobchenko[23], M. Böcker[27], A. Bogatyrev[23], G. Bohm[30], M. Bräuer[14], M. Bruinsma[29,1], M. Bruschi[6], P. Buchholz[27], T. Buran[25], J. Carvalho[9], P. Conde[2,13], C. Cruse[11], M. Dam[10], K. M. Danielsen[25], M. Danilov[23], S. De Castro[6], H. Deppe[15], X. Dong[3], H. B. Dreis[15], V. Egorytchev[13], K. Ehret[11], F. Eisele[15], D. Emeliyanov[13], S. Essenov[23], L. Fabbri[6], P. Faccioli[6], M. Feuerstack-Raible[15], J. Flammer[13], B. Fominykh[23,†], M. Funcke[11], Ll. Garrido[2], A. Gellrich[30], B. Giacobbe[6], J. Gläß[21], D. Goloubkov[13,34], Y. Golubkov[13,35], A. Golutvin[23], I. Golutvin[12], I. Gorbounov[13,27], A. Gorišek[18], O. Gouchtchine[23], D. C. Goulart[8], S. Gradl[15], W. Gradl[15], F. Grimaldi[6], J. Groth-Jensen[10], Yu. Guilitsky[23,36], J. D. Hansen[10], J. M. Hernández[30], W. Hofmann[14], M. Hohlmann[13], T. Hott[15], W. Hulsbergen[1], U. Husemann[27], O. Igonkina[23], M. Ispiryan[16], T. Jagla[14], C. Jiang[3], H. Kapitza[13,11], S. Karabekyan[26], N. Karpenko[12], S. Keller[27], J. Kessler[15], F. Khasanov[23], Yu. Kiryushin[12], I. Kisel[24], E. Klinkby[10], K. T. Knöpfle[14], H. Kolanoski[5], S. Korpar[22,18], C. Krauss[15], P. Kreuzer[13,20], P. Križan[19,18], D. Krücker[5], S. Kupper[18], T. Kvaratskheliia[23], A. Lanyov[12], K. Lau[16], B. Lewendel[13], T. Lohse[5], B. Lomonosov[13,33], R. Männer[21], R. Mankel[30], S. Masciocchi[13], I. Massa[6], I. Matchikhilian[23], G. Medin[5], M. Medinnis[13], M. Mevius[13], A. Michetti[13], Yu. Mikhailov[23,36], R. Mizuk[23], R. Muresan[10], M. zur Nedden[5], M. Negodaev[13,33], M. Nörenberg[13], S. Nowak[30], M. T. Núñez Pardo de Vera[13], M. Ouchrif[29,1], F. Ould-Saada[25], C. Padilla[13], D. Peralta[2], R. Pernack[26], R. Pestotnik[18], B. AA. Petersen[10], M. Piccinini[6], M. A. Pleier[14], M. Poli[6,32], V. Popov[23], D. Pose[12,15], S. Prystupa[17], V. Pugatch[17], Y. Pylypchenko[25], J. Pyrlik[16], K. Reeves[14], D. Reßing[13], H. Rick[15], I. Riu[13], P. Robmann[31], I. Rostovtseva[23], V. Rybnikov[13], F. Sánchez[14], A. Sbrizzi[1], M. Schmelling[14], B. Schmidt[13], A. Schreiner[30], H. Schröder[26], U. Schwanke[30], A. J. Schwartz[8], A. S. Schwarz[13], B. Schwenninger[11], B. Schwingenheuer[14], F. Sciacca[14], N. Semprini-Cesari[6], S. Shuvalov[23,5], L. Silva[9], L. Sözüer[13], S. Solunin[12], A. Somov[13], S. Somov[13,34], J. Spengler[13], R. Spighi[6], A. Spiridonov[30,23], A. Stanovnik[19,18], M. Starič[18], C. Stegmann[5], H. S. Subramania[16], M. Symalla[13,11], I. Tikhomirov[23], M. Titov[23], I. Tsakov[28], U. Uwer[15], C. van Eldik[13,11], Yu. Vassiliev[17], M. Villa[6], A. Vitale[6,7,†], I. Vukotic[5,30], H. Wahlberg[29], A. H. Walenta[27], M. Walter[30], J. J. Wang[4], D. Wegener[11], U. Werthenbach[27], H. Wolters[9], R. Wurth[13], A. Wurz[21], S. Xella-Hansen[10], Yu. Zaitsev[23], M. Zavertyaev[13,14,33], T. Zeuner[13,27], A. Zhelezov[23], Z. Zheng[3], R. Zimmermann[26], T. Živko[18], A. Zoccoli[6]

[1] NIKHEF, 1009 DB Amsterdam, The Netherlands [a]
[2] Department ECM, Faculty of Physics, University of Barcelona, E-08028 Barcelona, Spain [b]
[3] Institute for High Energy Physics, Beijing 100039, P.R. China
[4] Institute of Engineering Physics, Tsinghua University, Beijing 100084, P.R. China
[5] Institut für Physik, Humboldt-Universität zu Berlin, D-12489 Berlin, Germany [c,d]
[6] Dipartimento di Fisica dell' Università di Bologna and INFN Sezione di Bologna, I-40126 Bologna, Italy
[7] also from Fondazione Giuseppe Occhialini, I-61034 Fossombrone(Pesaro Urbino), Italy
[8] Department of Physics, University of Cincinnati, Cincinnati, Ohio 45221, USA [e]
[9] LIP Coimbra, P-3004-516 Coimbra, Portugal [f]
[10] Niels Bohr Institutet, DK 2100 Copenhagen, Denmark [g]
[11] Institut für Physik, Universität Dortmund, D-44221 Dortmund, Germany [d]
[12] Joint Institute for Nuclear Research Dubna, 141980 Dubna, Moscow region, Russia
[13] DESY, D-22603 Hamburg, Germany
[14] Max-Planck-Institut für Kernphysik, D-69117 Heidelberg, Germany [d]
[15] Physikalisches Institut, Universität Heidelberg, D-69120 Heidelberg, Germany [d]
[16] Department of Physics, University of Houston, Houston, TX 77204, USA [e]
[17] Institute for Nuclear Research, Ukrainian Academy of Science, 03680 Kiev, Ukraine [h]
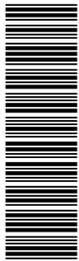
[18] *J. Stefan Institute, 1001 Ljubljana, Slovenia* [i]
[19] *University of Ljubljana, 1001 Ljubljana, Slovenia*
[20] *University of California, Los Angeles, CA 90024, USA* [j]
[21] *Lehrstuhl für Informatik V, Universität Mannheim, D-68131 Mannheim, Germany*
[22] *University of Maribor, 2000 Maribor, Slovenia*
[23] *Institute of Theoretical and Experimental Physics, 117218 Moscow, Russia* [k]
[24] *Max-Planck-Institut für Physik, Werner-Heisenberg-Institut, D-80805 München, Germany* [d]
[25] *Dept. of Physics, University of Oslo, N-0316 Oslo, Norway* [l]
[26] *Fachbereich Physik, Universität Rostock, D-18051 Rostock, Germany* [d]
[27] *Fachbereich Physik, Universität Siegen, D-57068 Siegen, Germany* [d]
[28] *Institute for Nuclear Research, INRNE-BAS, Sofia, Bulgaria*
[29] *Universiteit Utrecht/NIKHEF, 3584 CB Utrecht, The Netherlands* [a]
[30] *DESY, D-15738 Zeuthen, Germany*
[31] *Physik-Institut, Universität Zürich, CH-8057 Zürich, Switzerland* [m]
[32] *visitor from Dipartimento di Energetica dell' Università di Firenze and INFN Sezione di Bologna, Italy*
[33] *visitor from P.N. Lebedev Physical Institute, 117924 Moscow B-333, Russia*
[34] *visitor from Moscow Physical Engineering Institute, 115409 Moscow, Russia*
[35] *visitor from Moscow State University, 119992 Moscow, Russia*
[36] *visitor from Institute for High Energy Physics, Protvino, Russia*
[37] *visitor from High Energy Physics Institute, 380086 Tbilisi, Georgia*
[†] *deceased*

Abstract

Inclusive doubly differential cross sections $d^2\sigma_{pA}/dx_F dp_T^2$ as a function of Feynman-x (x_F) and transverse momentum (p_T) for the production of K_S^0, Λ and $\bar{\Lambda}$ in proton-nucleus interactions at 920 GeV are presented. The measurements were performed by HERA-B in the negative x_F range ($-0.12 < x_F < 0.0$) and for transverse momenta up to $p_T = 1.6$ GeV/c. Results for three target materials: carbon, titanium and tungsten are given. The ratios of production cross sections are presented and discussed. The Cronin effect is clearly observed for all three V^0 species. The atomic number dependence is parameterized as $\sigma_{pA} = \sigma_{pN} \cdot A^\alpha$ where σ_{pN} is the proton-nucleon cross section. The measured values of α are all near one. The results are compared with EPOS 1.67 and PYTHIA 6.3. EPOS reproduces the data to within $\approx 20\%$ except at very low transverse momentum.

PACS 13.85.Hd, 14.20.Jn, 14.40.Aq

1 Introduction

The study of strange particle production in proton in-
duced reactions has a long history, starting from the
discovery of strange particles in cosmic rays in the
1950s. Numerous studies have been made (see [1-20,
and references therein]) including fixed-target experi-
ments at Center-of-Mass (CM) energies up to 40 GeV,
mainly with bubble chambers, as well as at CERN's In-
tersecting Storage Ring in the 1970s and early 1980s (
see [21–24]) and later at the SPS Collider [25]. More
recently, studies of strangeness production at a CM en-
ergy of 200 GeV in both proton-proton and deuteron-
gold collisions at RHIC have been published [26, 27].
A detailed understanding of the underlying produc-
tion mechanism, particularly in proton-nucleus inter-
actions, is lacking. Further work, both experimental
and theoretical, is needed both to improve the model-
ing of atmospheric cosmic ray showers, and to serve as
a reference for strangeness production studies in heavy
ion collisions. The study presented in this paper was
performed at the highest available fixed-target energy
and benefits from a large sample size.

We present the doubly differential cross sections
for K_S^0, Λ, and $\bar{\Lambda}$ production in proton collisions with
carbon, titanium and tungsten targets at a CM en-
ergy of $\sqrt{s} = 41.6$ GeV as a function of the squared
transverse momentum range (p_T) in the range ($0 <
p_T^2 < 2.5 (\text{GeV/c})^2$) and Feynman-x ($x_F$) in the range
($-0.12 < x_F < 0.0$). The cross sections and derived
quantities are compared to predictions obtained from
PYTHIA 6.3 [28] and the EPOS 1.67 event genera-
tor [29]. PYTHIA is not designed to model proton-
nucleus interactions, but the comparison is nonetheless
instructive. EPOS is an event model currently under
development which has recently been shown to accu-
rately account for many features of proton-proton [26]
and deuteron-gold collisions at RHIC [29]. The EPOS
model is based on parton-parton interactions in which
cascades of usually off-shell partons ("parton ladders")
are produced which eventually hadronize into the ob-
served final state hadrons. More than one parton
ladder is generally produced. In the case of proton-
nucleus collisions, the partons representing the ladder
rungs can "rescatter" with other target nucleons via
elastic or inelastic interactions. This leads to increased
screening and also p_T broadening with increasing tar-
get mass number.

In the following sections we briefly describe the de-
tector, the analysis and finally present the results. The
study presented here supersedes the previously pub-
lished HERA-B study [30] whose results are inconsis-
tent with those presented herein largely due to errors
in the detector description used for the previous study.

2 HERA-B experiment and data sample

HERA-B was a fixed target experiment at the proton
storage ring of HERA at DESY [31]. Collisions were
produced by inserting one or more wire targets into
the halo of the 920 GeV/c proton beam. The center-
of-mass energy in the proton-nucleon system was $\sqrt{s} =
41.6$ GeV.

The detector was designed and built as a mag-
netic spectrometer with a forward acceptance of 15-
220 mrad in the bending (horizontal) and 15-160 mrad
in the non-bending (vertical) plane. The target sys-
tem [32] consisted of two stations separated by about
5 cm with four wires each. The wires were posi-
tioned above, below, and on either side of the beam
and were made of various materials including carbon,
titanium and tungsten. The vertex detector system
(VDS) [33] was a planar micro-strip vertex detector
providing a precise measurement of primary and sec-
ondary vertices. The VDS consisted of 8 stations (with
4 stereo views each) of double-sided silicon strip detec-
tors mounted in movable Roman Pots which allowed
operation as near as 10 mm from the beam and pro-
vided for retraction during beam manipulations. The
vacuum vessel housing the detector was an integral
part of the HERA proton ring. The VDS was fol-
lowed by a large aperture dipole magnet with a field
integral of 2.13 Tm, and a set of tracking chambers
(OTR) [34] consisting of ≈95,000 channels of honey-
comb drift cells. Particle identification was performed
by a Ring Imaging Cherenkov detector [35], an elec-
tromagnetic calorimeter [36] and a muon system [37].

This analysis is based on about 10^7 interactions on
each of carbon, titanium and tungsten targets. The
data set is a subsample of the full minimum bias data
set ($2 \cdot 10^8$ events) which was taken over a three-day pe-
riod from a single filling of protons in the HERA pro-
ton ring to minimize systematic uncertainties. Only
one of the three target wires was in use at a time.
All data were recorded with an interaction rate of
1.5 MHz, corresponding to about one inelastic interac-
tion per six bunch crossings. Non-empty events were
selected using an interaction trigger which required at
least 20 hits in the RICH detector (compared to an av-
erage of 33 for a full ring from a $\beta = 1$ particle [35]) or
an energy deposit of at least 1 GeV in the electromag-
netic calorimeter. The trigger was sensitive to more
than 97% of the total inelastic cross section σ_{inel} [39].
The data sample also includes about $5 \cdot 10^5$ events
per target selected at random, with no trigger require-
ment, which were taken at a 10 Hz rate throughout the
data taking period. These "random" events were used
for luminosity determination and systematic studies.

The entire V^0 candidate reconstruction chain was based exclusively on information from the VDS and OTR. All events were reconstructed with the standard HERA-B analysis package [40].

3   Data analysis

The K_S^0, Λ and $\bar{\Lambda}$ particles are reconstructed from their two particle decays $K_S^0 \to \pi^+\pi^-$, $\Lambda \to p\pi^-$ and $\bar{\Lambda} \to \bar{p}\pi^+$, respectively.

For this analysis, a track consists of matched reconstructed OTR and VDS track segments. A search for a primary vertex is performed using them and, if successful, the interaction point is taken to be the location of the found vertex. If unsuccessful, the position of the target wire together with the average position of interactions along the wire are used. In each event, a full combinatorial search for V^0 candidates is then performed.

V^0 candidates are selected from all pairs of oppositely charged tracks which form a secondary vertex downstream of the interaction point. The minimum distance between the two tracks of a pair is required to be less then 0.14 cm. The $\pi^+\pi^-$, $p\pi^-$ and $\bar{p}\pi^+$ mass hypotheses are assigned in turn. If the $\pi^+\pi^-$ invariant mass hypothesis lies in the region $0.44 < M_{\pi^+\pi^-} < 0.56\,\text{GeV/c}^2$ or either the $p\pi^-$ or $\bar{p}\pi^+$ invariant mass hypothesis lie in the region $1.09 < M_{p\pi^-/\bar{p}\pi^+} < 1.14\,\text{GeV/c}^2$, the pair is accepted for further analysis. To reduce cross-contamination of K_S^0's and $\Lambda/\bar{\Lambda}$ samples, pairs with $\pi^+\pi^-$ invariant mass in the range $0.476 < M_{\pi^+\pi^-} < 0.515\,\text{GeV/c}^2$ are excluded from the Λ and $\bar{\Lambda}$ analyses, and pairs with $p\pi^-$ and $\bar{p}\pi^+$ mass hypotheses in the range $1.109 < M_{p\pi^-/\bar{p}\pi^+} < 1.121\,\text{GeV/c}^2$ are excluded from the K_S^0 analysis.

Finally, a cut on the product of the transverse momenta of the decay products relative to the flight direction of the V^0 candidate and the proper decay length of the V^0, $\tilde{p_T} \cdot c\tau > 0.05$ GeV/c $\cdot$ cm, is applied. This requirement rejects short-lived combinatorial background from the target region and also reduces background from $\gamma \to e^+e^-$ conversions.

The final invariant mass distributions for selected K_S^0, Λ, and $\bar{\Lambda}$ candidates from the carbon target sample are shown in Fig. 1. Distributions from the other samples are similar. The signals are clearly seen above a smooth background. The yields of V^0 are calculated from the number of entries in each bin of the signal region within a $\pm 4\sigma$ window around the peak position minus the background, which is taken from the left and right sidebands with a width of 4σ each. A fit to

Table 1: The number of inelastic events (N_{evt}), number of reconstructed V^0 (N_{V^0}) and the integrated luminosities [39] $\mathcal{L}_A$ in mb^{-1} for the indicated targets.

	C	Ti	W
N_{evt}	9350000	9790000	10900000
$N_{K_S^0}$	152260 ± 550	210780 ± 780	265800 ± 860
N_Λ	30800 ± 270	45170 ± 350	65170 ± 440
$N_{\bar{\Lambda}}$	15220 ± 240	20990 ± 310	28840 ± 430
$\mathcal{L}_A$	$40900. \pm 1600.$	$14880. \pm 520.$	$6110. \pm 200.$

the mass spectra using two Gaussians with a common mean to describe the signal and a first order polynomial to describe the background gives central mass values of 497.0 MeV, 1115.3 MeV and 1115.9 MeV for K_S^0, Λ, and $\bar{\Lambda}$, respectively; all well within 1 MeV of the current PDG values [38].

The number of inelastic events, the signal yields obtained from the selection described above, and the luminosity values [39] are summarized in Table 1 for each target material.

4   Acceptance and visible kinematic region

The reconstruction efficiencies for K_S^0, Λ and $\bar{\Lambda}$ in the selected decay channels are determined from Monte Carlo (MC) using the FRITIOF 7.02 package [42] for event generation. FRITIOF is a proton-proton, proton-nucleus and nucleus-nucleus collision generator based on a model in which hadrons are treated as strings. The generated events are propagated through the detector using the GEANT 3.21 package [43]. Realistic detector efficiencies, electronic noise and dead channel maps are included in the simulation. The MC events are processed through the same reconstruction chain as the data. The sizes of the MC samples used for the efficiency calculations are about the same as those of the data. The uncertainties due to MC statistics are added in quadrature with the statistical uncertainties of the data.

The total efficiency which includes geometric acceptance, track reconstruction efficiency, and the efficiency of selection cuts, depends on the kinematic variables and is, on average, 9% for K_S^0, and 5% for Λ and $\bar{\Lambda}$ inside the "visible region", defined as $-0.12 < x_F < 0.0$ and $p_T^2 < 2.5\,\text{GeV}^2/\text{c}^2$, for all V^0
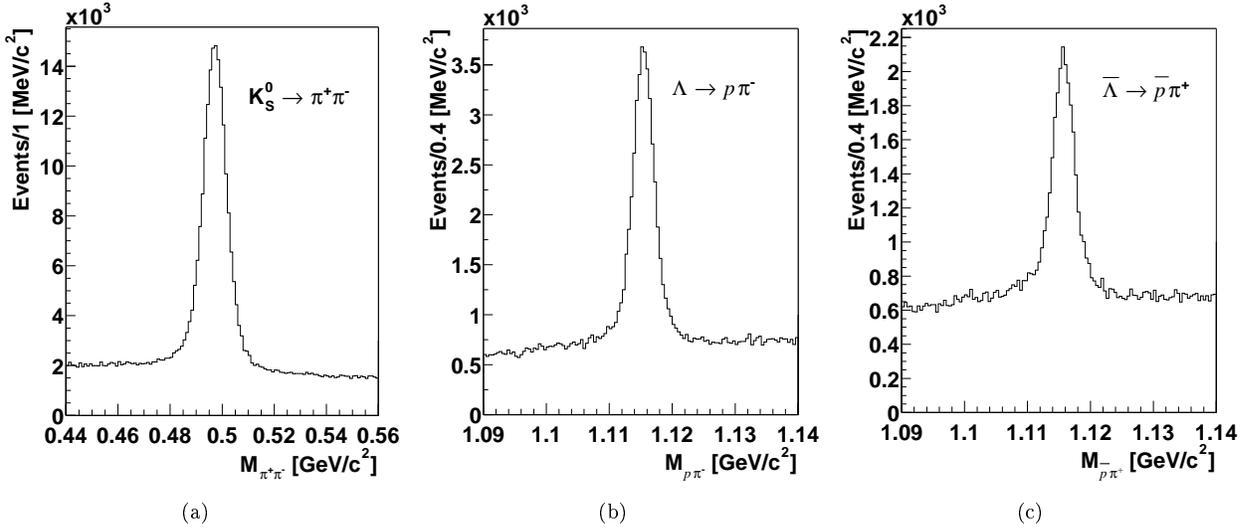
Figure 1: The invariant mass distributions for oppositely charged particle pairs, assuming a) $\pi^+\pi^-$, b) $p\pi^-$ and c) $\bar{p}\pi^+$ mass assignments for the carbon target sample after application of the selection criteria described in the text.

types. The efficiencies are determined on a grid in x_F and p_T^2 with 6 equal bins in x_F and 10 equal bins in p_T^2 over the range given above, for a total of 60 bins. The grid-based acceptance correction has the advantage of minimizing any biases due to inaccuracies in the generated kinematic distributions.

For K_S^0 mesons, the low p_T bins of the lowest x_F regions are poorly populated due to low acceptance, and are therefore excluded. Specifically, for a bin to be considered, we require that it contain at least 10 events in both MC and data samples. For K_S^0 mesons, the x_F/p_T^2 interval $[-0.12, -0.08]$ / $[0.0, 0.5]$ GeV/c^2 for all samples and in addition the interval $[-0.12, -0.10]$ / $[0.5, 0.75]$ GeV/c^2 for the titanium sample are excluded. For the total cross section, A-dependence, and production-ratio studies, the data are summed either in slices of x_F or p_T^2. The results are limited to the kinematic range over which all bins are populated. Thus, for the K_S^0, only the x_F interval $-0.08 < x_F < 0.0$ is considered for such studies.

Based on a MC study, a small correction is applied to account for those V^0 particles which are produced in interactions with the detector material. The corrections obtained reduce the acceptance by 0.9%–1.2% for K_S^0, 1.0%–1.4% for Λ and 0.3% for $\bar{\Lambda}$, depending on target material.

5 Experimental results

The main results of this paper, the doubly differential cross sections, are discussed in the following section. The subsequent sections are devoted to discussions of quantities derived from these numbers, such as A-dependence and production ratios.

5.1 Doubly differential cross sections

The doubly differential cross section for the state V^0 in the (i,j)th bin of (x_F, p_T^2) is computed from the following formula:

$$\frac{d^2\sigma_{pA}^{V^0}(i,j)}{dx_F dp_T^2} = \frac{N_{i,j}^{V^0}}{Br(V^0) \cdot \mathcal{L}_A \cdot \epsilon_{i,j}^{V^0} \cdot \Delta x_F \cdot \Delta p_T^2}, \quad (1)$$

where $Br(V^0)$ [38] is the branching ratio of the detected decay and $\mathcal{L}_A$ is the integrated luminosity of the data set for the specified target material (see Table 1). $N_{i,j}^{V^0}$ is the background-subtracted number of reconstructed V^0 candidates in the (i,j)th bin of (x_F, p_T^2) and $\epsilon_{i,j}^{V^0}$ is the corresponding efficiency calculated from the MC as described in Sect. 4. The bin widths are 0.02 in x_F and 0.25 GeV/c^2 in p_T.

The values of the inclusive doubly differential cross sections, $d^2\sigma/dx_F dp_T^2$ for the full visible region are reported in Tables 6, 7 and 8 for all three target materials and illustrated in Fig. 2. The measurement resolutions in x_F and p_T^2 are small compared to the bin width. A discussion of systematic uncertainties can be found in
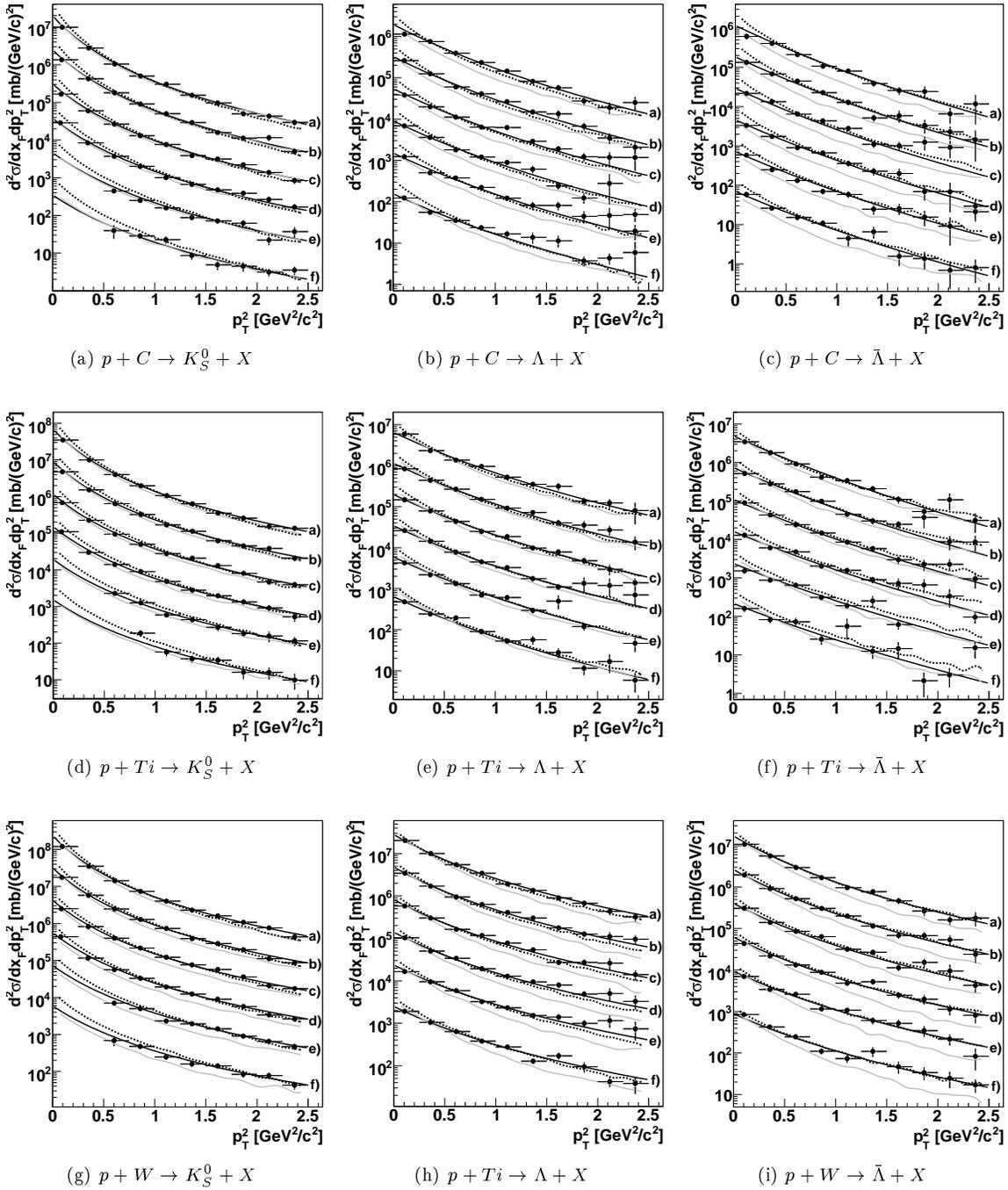
(a) $p + C \rightarrow K_S^0 + X$

(b) $p + C \rightarrow \Lambda + X$

(c) $p + C \rightarrow \bar{\Lambda} + X$

(d) $p + Ti \rightarrow K_S^0 + X$

(e) $p + Ti \rightarrow \Lambda + X$

(f) $p + Ti \rightarrow \bar{\Lambda} + X$

(g) $p + W \rightarrow K_S^0 + X$

(h) $p + Ti \rightarrow \Lambda + X$

(i) $p + W \rightarrow \bar{\Lambda} + X$

Figure 2: The measured inclusive doubly differential cross section $d^2\sigma_{pA}/dx_F dp_T^2$ vs. p_T^2 in 6 x_F slices for K_S^0, Λ , and $\bar{\Lambda}$ production on carbon, titanium and tungsten targets. The error bars indicate the statistical uncertainties only. For display purposes, the cross sections in each x_F slice have been multiplied by the following numbers (the letters correspond to those on the right of each curve): a) 5000, b) 1000, c) 200, d) 40, e) 8, f) 1. The x_F ranges for each curve correspond to those given in Tables 6, 7 and 8: a) -0.02 − 0, b) -0.04 − -0.02, c) -0.06 − -0.04, d) -0.08 − -0.06, e) -0.10 − -0.08, f) -0.12 − -0.10. The parameterizations discussed in the text are shown as dark solid lines. The light solid lines show the results of PYTHIA normalized to the (x_F, p_T^2) bin (-0.01, 0.125 $(GeV/c)^2$) (separately for each plot). EPOS results are indicated by dashed lines.

Table 2: Results of the combined power-law fits (Eq. 2) for the doubly differential cross sections $d^2\sigma_{pA}/dx_F dp_T^2$. Data were fitted in the acceptance region ($-0.12 < x_F < 0.0$ and $0.0 < p_T^2 < 2.5\,\mathrm{GeV^2/c^2}$). Systematic uncertainties were not included in the fit and empty cells were excluded.

	C_0 [mb/(GeV/c)^2]	β	A, [GeV^2/c^2]	B, [GeV^2/c^2]	n	χ^2/DOF
			$p + A \to K_S^0 + X$			
C	$4893. \pm 79.$	3.93 ± 0.09	0.53 ± 0.02	3.57 ± 0.32	22.85 ± 0.64	$81./51$
Ti	$16650. \pm 270.$	3.69 ± 0.08	0.50 ± 0.02	2.89 ± 0.32	20.71 ± 0.70	$40./50$
W	$56980. \pm 770.$	3.53 ± 0.06	0.48 ± 0.01	3.12 ± 0.28	19.53 ± 0.58	$91./51$
			$p + A \to \Lambda + X$			
C	$425. \pm 21.$	6.90 ± 0.96	2.33 ± 0.43	2.4 ± 1.4	8.64 ± 0.67	$91./55$
Ti	$1402. \pm 52.$	6.40 ± 0.87	2.33 ± 0.41	0	6.62 ± 0.35	$59./54$
W	$6040. \pm 260.$	3.98 ± 0.31	1.19 ± 0.15	2.34 ± 0.63	7.57 ± 0.56	$62./55$
			$p + A \to \bar{\Lambda} + X$			
C	$259. \pm 19.$	9.9 ± 2.6	3.4 ± 1.2	3.8 ± 3.2	11.3 ± 1.0	$72./54$
Ti	$1121. \pm 82.$	11.0 ± 3.2	3.8 ± 1.6	7.0 ± 4.6	14.2 ± 1.2	$63./52$
W	$3860. \pm 270.$	4.86 ± 0.59	1.40 ± 0.26	4.4 ± 1.4	12.6 ± 1.0	$59./55$

Sect. 6. For the excluded bins (see Sect. 4), the values reported in the tables were extrapolated using the fits described below.

The measured cross section distributions have the same general behavior for all V^0 particles and can be described by the following parameterization:

$$\frac{d^2\sigma}{dx_F dp_T^2} = C_0 \cdot (1 - |x_F|)^n \cdot \left(1 + \frac{p_T^2}{A + B \cdot |x_F|}\right)^{-\beta}. \tag{2}$$

The power law parameterization in x_F is often used, particularly in the fragmention region where the measured power has been used to distinguish fragmentation models [44]. While the parametrization has no theoretical underpinning in the x_F range of the present measurement, it nonetheless gives a good representation of the data. The parameterization of the p_T dependence is also often seen in the literature, except that we have found it necessary to introduce a linear term in $|x_F|$ into the factor dividing p_T^2 since the distributions tend to flatten with decreasing x_F. This is the well-known "sea-gull" effect [45] first observed [46] in bubble chamber experiments. The fitted curves are shown as dark solid lines in Fig. 2 and the fit parameters together with the fit χ^2s are summarized in Table 2. The functions are in agreement with the data at the level of 5% or better in the high statistics bins and otherwise compatible with the data within statistical errors.

The reported values for the parameter n are for the most part considerably larger than either those expected by the counting rules given in [44] or the measurements summarized in the same paper. However, as noted above, the model of [44] applies only for x_F values outside the measured x_F range. Both Pythia and EPOS indicate that n is a strong function of x_F with n close to the numbers reported in Table 2 for $|x_F| \lesssim 0.1$ but decreasing to values similar to those given in [44] for $|x_F| \approx 0.5$. The fitted functions have been used to calculate the values of the doubly differential cross section in the unmeasured bins of the grid. These values are presented in Table 6, 7 and 8 (marked by asterisks).

The results of PYTHIA and EPOS are indicated in Fig. 2 by light solid lines and dotted lines, respectively. The PYTHIA results are for proton-proton collisions at $\sqrt{s} = 41.6\,\mathrm{GeV}$ (with default settings) and therefore the total calculated cross sections do not correspond to the measured pA cross sections. Thus, to facilitate the comparison of shapes, the normalizations are arbitrarily adjusted such that the PYTHIA results agree with the data in the highest x_F and lowest p_T^2 bin of each plot separately. In contrast, EPOS provides the cross section relative to the total inelastic cross section for each target. The inelastic cross sections are taken from [39].

As expected, the EPOS calculations generally give a better description of the data than the (arbitrarily normalized) PYTHIA curves although PYTHIA is remarkably good at describing the K_S^0 data for the lighter target materials. Since the PYTHIA calculations are for proton-proton interactions, they can be expected to give a progressively poorer description of the data with increasing A, at least in part due to the Cronin effect [47]: the flattening of the p_T distribution with increasing atomic mass number. In general, the EPOS curves give a quite satisfactory description of
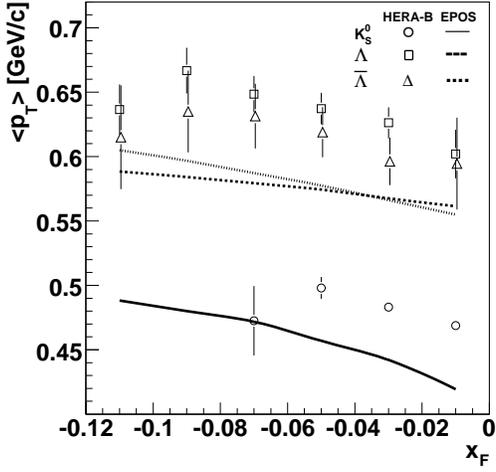
7

Figure 3: The average transverse momentum, $\langle p_T \rangle$, of K_S^0, Λ, and $\bar{\Lambda}$ as a function of x_F from the tungsten target sample (points) together with the EPOS data (lines). Error bars are statistical only.

the data (to better than $\approx 20\%$ for most of the measured range) although there is a pronounced tendency to overestimate the cross section at low-p_T, particularly for the lighter targets.
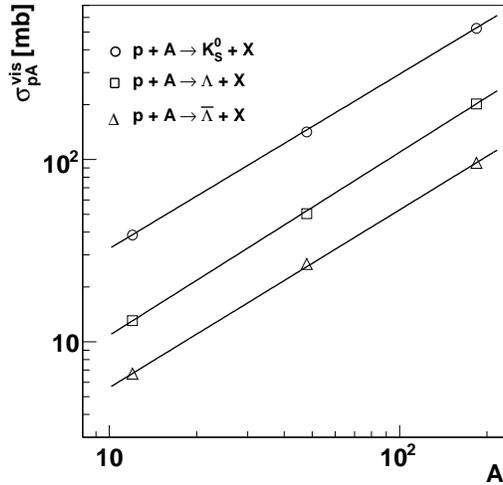

Figure 4: Atomic mass number dependences of the V^0 integrated inclusive cross sections σ_{pA}^{vis}. The solid lines represent fits to the parameterization (Eq. 4). The uncertainties include both statistical and systematic contributions.

The average transverse momentum in a specific (x_{F_i}) slice can be calculated using the formula:

$$\langle p_{T_i} \rangle = \frac{\sum_{j=1}^{n} \langle p_T \rangle_{i,j} \cdot \sigma_{i,j}}{\sum_{j=1}^{n} \sigma_{i,j}}, \qquad (3)$$

where the average p_T in the (i,j)'th bin, $\langle p_{T_{i,j}} \rangle$, is calculated from the parameterization (Eq. 2), $\sigma_{i,j}$ is the

Table 3: The integrated inclusive differential production cross sections σ_{pA}^{vis} in the acceptance of the measurement. The uncertainties are statistical. The acceptance boundaries of the measurement in x_F and p_T^2 are given in the 3rd and 4th columns, respectively.

	x_F interval	p_T^2 range, [GeV^2/c^2]	σ_{pA}^{vis}, [mb]
$p + A \to K_S^0 + X$			
C			38.5 ± 0.4
Ti	$-0.08 - 0.0$	$0.0 - 2.5$	141.8 ± 1.9
W			523.9 ± 5.4
$p + A \to \Lambda + X$			
C			13.1 ± 0.2
Ti	$-0.12 - 0.0$	$0.0 - 2.5$	50.5 ± 0.7
W			201.7 ± 2.1
$p + A \to \bar{\Lambda} + X$			
C			6.7 ± 0.2
Ti	$-0.12 - 0.0$	$0.0 - 2.5$	26.7 ± 0.6
W			95.7 ± 1.9

value of the cross section in the same bin, and n is the number of (p_T^2) bins. This quantity is plotted in Fig. 3 as a function of x_F for K_S^0, Λ, and $\bar{\Lambda}$ for the tungsten target sample together with the corresponding EPOS predictions. The EPOS predictions show the same trend of increasing $\langle p_T \rangle$ with decreasing x_F as the data and also the same ordering with $\langle p_T \rangle$: $\langle p_T \rangle$ of Λ slightly higher than the $\langle p_T \rangle$ of $\bar{\Lambda}$ which is higher than the $\langle p_T \rangle$ of K_S^0, although the averages are slightly underestimated. The average p_T from carbon and titanium samples behave similarly (not shown).

5.2 Integrated cross section and atomic mass number dependence

The inclusive production cross section in the visible region is computed by summing the differential cross sections over all bins. The results, σ_{pA}^{vis}, are listed in Table 3. According to the fitted functional forms, the measured cross sections correspond to more than 98% of the total cross section in the visible x_F interval for all targets and all V^0 particles.

The dependence of the measured cross sections σ_{pA}^{vis} on the atomic mass of the target material (A) can be described by a power-law:

$$\sigma_{pA}^{vis} \propto A^{\alpha^{vis}}, \qquad (4)$$

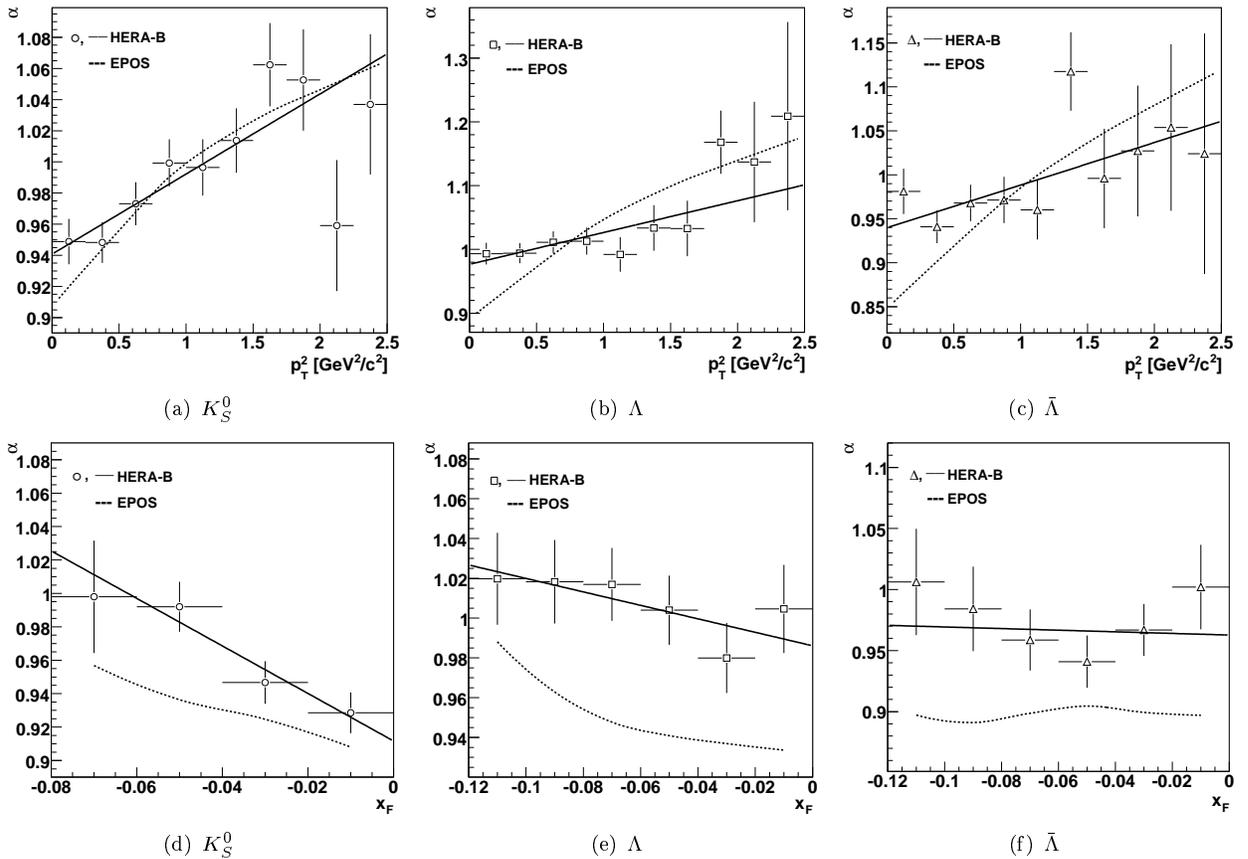where, in this case, α^{vis} characterizes the average atomic mass number dependence of the visible cross

(a) K_S^0 (b) Λ (c) $\bar{\Lambda}$

(d) K_S^0 (e) Λ (f) $\bar{\Lambda}$

Figure 5: The dependence of α for K_S^0, Λ and $\bar{\Lambda}$ production on p_T^2 (top plots) and x_F (bottom plots). The points show the measured values and the solid lines are the results of straight-line fits to the data. EPOS calculations are shown as dotted lines. The uncertainties include both statistical and systematic contributions.

section. The systematic uncertainties on the individual cross section measurements are highly correlated between the target materials, therefore the least-squares likelihood function used to extract σ_{pA} and α uses the full error matrix of the measurements. The visible cross sections, together with the fitted curves are shown in Fig. 4. The fit results and χ^2s are given in Table 4.

The dependences of α on p_T^2 and on x_F are shown on Fig. 5. The solid lines are from straight-line fits whose parameters are given in Table 4 and the dashed lines are the EPOS predictions. The Cronin effect manifests itself as an increase of α with increasing p_T. The EPOS curves reproduce the p_T dependence rather well except for the first p_T bins where EPOS underestimates α. Since the main contributions to the cross sections are at low p_T, the EPOS predictions lie well under the data points in the α vs. x_F plots although the trends with x_F is the same within errors.

The total cross sections (also given in Table 4) are found be dividing the visible cross sections by the frac-

tion of the total cross section in the visible region. This fraction was estimated using an average of EPOS results for the fractions of all V^0s produced in proton-proton and proton-neutron interactions in the measured x_F interval (34.7%, 17.5% and 35.4% for K_S^0, Λ and $\bar{\Lambda}$, respectively). The alternative of separately correcting each proton-nucleus cross section before extrapolation to $A = 1$ was rejected since it relies more heavily on the Monte Carlo.

5.3   Particle ratios

The ratio of the $\bar{\Lambda}$ cross section to that of the Λ is plotted in Fig. 6 as functions of x_F and p_T^2 for the three targets. For Fig. 6a, the data have been summed over the full measured p_T^2 range, and for Fig. 6b, over the full x_F range. The EPOS calculations are also shown. The PYTHIA result indicated in Fig. 6b, is well above the data. The PYTHIA result vs. x_F is well above the upper plot boundary in Fig. 6a, starting at ≈ 0.8 at $x_F \approx -0.1$, and increasing smoothly to
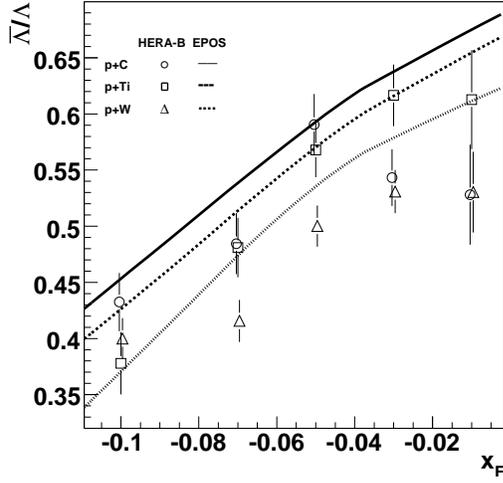
(a) $\bar{\Lambda}/\Lambda$ vs. x_F
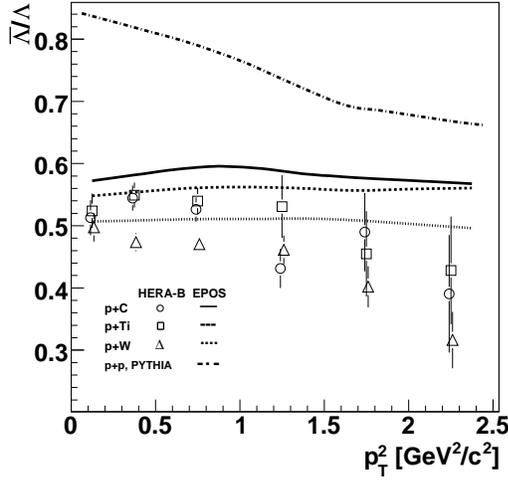
(b) $\bar{\Lambda}/\Lambda$ vs. p_T

Figure 6: The ratios of $\bar{\Lambda}/\Lambda$: a) vs. x_F and b) vs. p_T^2. The points show the measured values and the various lines indicate the predictions of PYTHIA (part b only) and EPOS. The PYTHIA prediction corresponding to part (a) is well above the upper plot boundary (see text). The error bars show statistical uncertainties only.

Table 4: The integrated V^0 production cross sections per nucleon σ_{pN}^{vis} in millibarns in the visible region and the values of α from the fit of the cross sections per nucleus to Eq. 4. The uncertainties include both statistical and systematic contributions. The results of fits to the data points in Fig. 5 are also given.

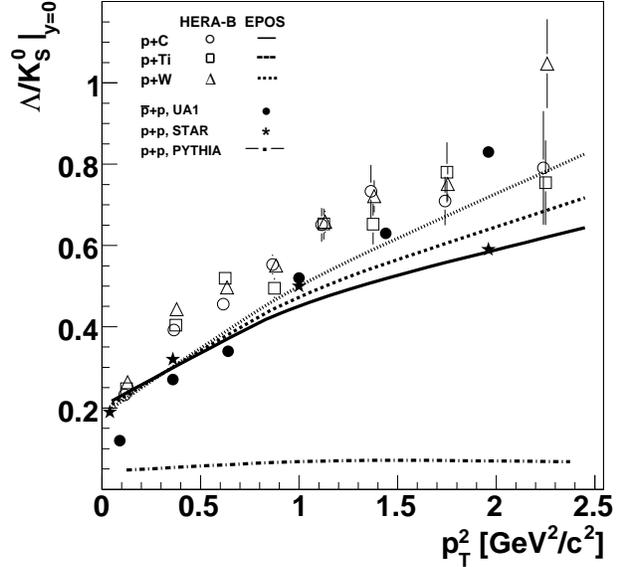|	K_S^0	Λ	$\bar{\Lambda}$
$\sigma_{pN\,[\mathrm{mb}]}^{vis}$	3.56 ± 0.33	1.07 ± 0.11	0.594 ± 0.080
$\sigma_{pN\,[\mathrm{mb}]}^{tot}$	10.33 ± 0.90	6.13 ± 0.61	1.68 ± 0.21
α^{vis}	0.957 ± 0.013	1.004 ± 0.016	0.975 ± 0.021
χ^2	0.4	0.9	0.5
Fits of Figs. 5a,b,c to $\alpha = \alpha_0^{p_T} + \alpha_1^{p_T} \cdot p_T$			
$\chi^2/_{\mathrm{DOF}}$	$8.4/8$	$7.8/8$	$10./8$
$\alpha_0^{p_T}$	0.941 ± 0.011	0.975 ± 0.015	0.938 ± 0.018
$\alpha_1^{p_T}$	0.052 ± 0.005	0.052 ± 0.007	0.052 ± 0.011
Fits of Figs. 5d,e,f to $\alpha = \alpha_0^{x_F} + \alpha_1^{x_F} \cdot x_F$			
$\chi^2/_{\mathrm{DOF}}$	$0.5/2$	$1.5/4$	$3.6/4$
$\alpha_0^{x_F}$	0.911 ± 0.021	0.986 ± 0.017	0.962 ± 0.025
$\alpha_1^{x_F}$	-1.43 ± 0.54	-0.346 ± 0.007	-0.072 ± 0.011

Figure 7: The ratios of Λ/K_S^0 vs. p_T^2 at $y \sim 0$. The open points show the measured values and the solid points show the results from STAR and UA1 collaborations. The various lines indicate the predictions of PYTHIA and EPOS. The error bars include only statistical contributions.

≈ 0.92 at $x_F \approx 0$. The EPOS result is in reasonable agreement with the data in Fig. 6a, where it is also seen to reproduce the A-dependence fairly well, despite the fact that the EPOS calculation of average α is well below the data for both Λ and $\bar{\Lambda}$ (see Figs. 5b and 5c). As illustrated in Fig. 6b, the EPOS curve is also in reasonable agreement with the data over most of the p_T^2 range but the data shows a tendency to decrease with p_T^2 while EPOS suggests a flat p_T^2 dependence.

The ratio of Λ to K_S^0 cross sections is shown in Fig. 7 for the three target materials. The STAR measurements [26] in pp interactions at $\sqrt{s} = 200\,\mathrm{GeV}$ and UA1 [25] in $\bar{p}p$ interactions at $\sqrt{s} = 630\,\mathrm{GeV}$ are also shown. The ratio shows no appreciable dependence on center-of-mass energy, atomic number or the type of colliding particles over the measured range. The EPOS results agree well with the data at low p_T but tend to underestimate the data at higher p_T. Nonetheless, as indicated in the figure, the EPOS calculation lies far closer to the data than the PYTHIA result over the full measured range.

5.4 Comparison with existing data

Only two experiments [21, 23] have measured V^0 production at a similar energy and in kinematic ranges which overlap with the present measurement. The first of these measurements, by Büsser et al., gives the average invariant cross section as a function of p_T of three separate measurements at $\sqrt{s} = 30.6$, 44.8, and 52.7 GeV (an average energy of 44 GeV) in proton-proton collisions and in a center-of-mass rapidity (y) interval of about 2 units centered at 0 and for p_T larger than $1.2\,\mathrm{GeV/c}(K_S^0)$ and $0.8\,\mathrm{GeV/c}$ (Λ and $\bar{\Lambda}$). The measurements are shown in Fig. 8. The second report, by Drijard et al. [23] gives invariant cross sections for K_S^0, Λ, and $\bar{\Lambda}$ over a wide range in rapidity and p_T in proton-proton collisions at $\sqrt{s} = 63\,\mathrm{GeV}$. The relevant points are also shown in Fig. 8. The HERA-B measurements are indicated in Fig. 8 by curves which are derived from the parameterization given by (Eq. 3). The fit parameters are fixed to those of the carbon target (Table 2) and the resulting values are extrapolated to $A = 1$ assuming the straight line fits to the α vs. p_T points shown in Fig. 5.

While the K_S^0 cross sections of [21] are in rather good agreement with the HERA-B results, the HERA-B Λ and $\bar{\Lambda}$ measurements are somewhat higher. Büsser et al. also extrapolate their measurements to $p_T = 0$ and report $(\frac{d\sigma}{dy})_{y=0} = 0.43 \pm 0.05\,\mathrm{mb}$ (Λ) and $0.27 \pm 0.04\,\mathrm{mb}$ ($\bar{\Lambda}$). The corresponding numbers for the present measurement, $(\frac{d\sigma}{dy})_{y=0} = 0.77 \pm 0.05\,\mathrm{mb}$ (Λ) and $(0.47 \pm 0.04\,\mathrm{mb}$ ($\bar{\Lambda}$) are nearly a factor of two
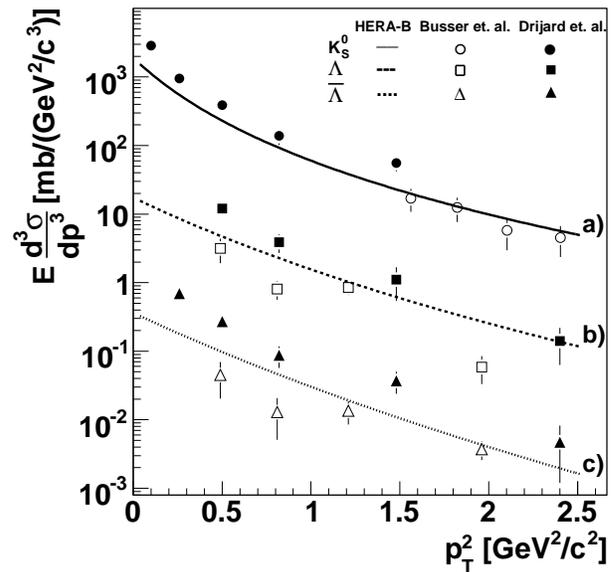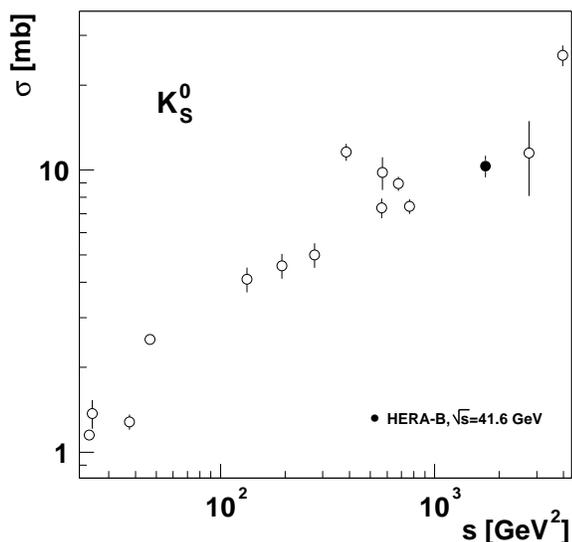

Figure 8: The average invariant cross section in the $|y| \lesssim 1$ interval for K_S^0, Λ, and $\bar{\Lambda}$ multiplied by the following scale factors: a) 600, b) 30, c) 1. The points are from [21] and [50]. The curves correspond to parameterizations of the present measurements as explained in the text.

higher. As shown in Fig. 8, the $y = 0$ measurements of [50] are also about a factor of two higher than the present measurement. This is, at least in part, explained by the substantially higher center-of-mass energy of the Drijard et al. measurements, however possible problems with the K_S^0 measurements reported in [23] have been noted [30] elsewhere.
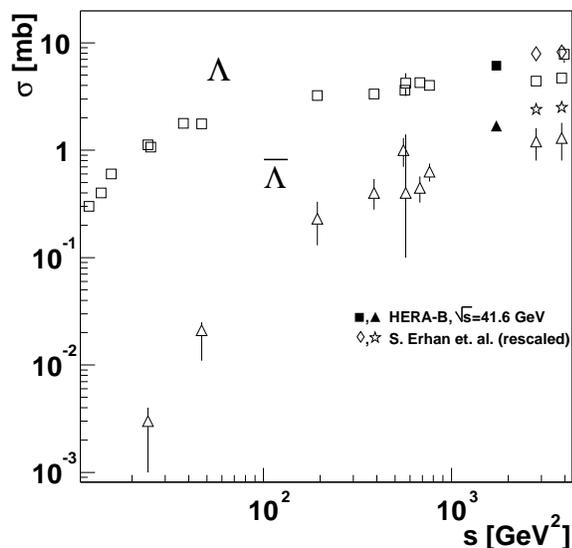
Finally, in Fig. 9, we show the HERA-B results together with previously published values of the total proton-nucleon cross section as a function of squared CM energy (s). The HERA-B results fit with the general trend of the data. Two notable exceptions are the two points at $s = 2800\,\mathrm{GeV}$ and $3800\,\mathrm{GeV}$ indicated by squares (Λ) and triangles ($\bar{\Lambda}$) from Erhan et al. [22] for Λ and $\bar{\Lambda}$ production. We note however that these points depend sensitively on the extrapolations of Büsser et al. [21] and that a multiplicative factor of two is missing from the transformation given in [22] of the Büsser et al. points from $d\sigma/dy$ to $d\sigma/d|x_F|$ [51]. If our own measurements are substituted for the Büsser et al. extrapolations, we estimate that the total cross section values of Erhan et al. would increase by about a factor of two and a more satisfactory agreement among the different measurements would result, as indicated by the recalculated points in the figure.

(a)

(b)

Figure 9: A compilation of total cross section measurements from references [6-24] and HERA-B for a) K_S^0 and b) Λ and $\bar{\Lambda}$ production vs. squared CM energy (s). The recalculated data from Erhan et al. [22] are indicated by diamonds and stars.

	K_S^0	Λ	$\bar{\Lambda}$
signal counting	3.2%	3.3%	4.5%
cut variation	0.4%	3.9%	5.2%
tracking efficiency	3.0%	3.0%	3.0%
branching ratio	0.05%	0.5%	0.5%
MC model	3.3%	3.7%	5.7%
total (w/o luminosity)	5.5%	7.0%	9.4%
	C	Ti	W
luminosity (tot)	5.0%	5.2%	4.2%
luminosity (uncorrelated)	3.9%	4.2%	2.9%

6 Systematic uncertainties and checks

The following possible sources of systematic uncertainty have been considered:

- A bin-based method is used for estimating the number of produced V^0 candidates. An alternative fit-based method in which the invariant mass distributions are fit to a double Gaussian for the signal and a first-order Legendre polynomial for the background results in changes to the cross sections of 3.2% for K_S^0, 3.3% for Λ and 4.5% for $\bar{\Lambda}$.

- From varying the most powerful cut, namely the cut on $\tilde{p}_T \cdot c\tau$, within reasonable limits, we estimate a systematic uncertainty of about 3.9% for Λ, 5.2% for $\bar{\Lambda}$ and 0.4% for K_S^0 mesons.

- The efficiencies for reconstruction of track segments in the VDS and in the OTR were measured independently by exploiting $\pi^+\pi^-$ decays [49] of the K_S^0. One of the two decay pions was reconstructed using RICH and ECAL information instead of either the OTR hits or the VDS hits and a search was made among the reconstructed tracks for a match. Based on a comparison of this method applied to data and to Monte Carlo, a systematic uncertainty on track reconstruction and matching efficiency of 1.5% per track is estimated.

- The influence of the track multiplicity on the reconstruction efficiency is found to give a negligible contribution to the systematic uncertainty.

- The systematic uncertainties on the branching ratios [38] are 0.05% for $K_S^0 \to \pi^+\pi^-$ and 0.5% for $\Lambda \to p\pi^-$ and $\bar{\Lambda} \to \bar{p}\pi^+$ decays, respectively.

- The total systematic uncertainties due to the luminosity calculations [39] are 5.0%, 5.2% and 4.2% for carbon, titanium and tungsten targets, respectively. The uncertainties are correlated between target materials with correlation coefficients varying between 0.90 and 0.92. For the A-dependence and pN cross section results, these uncertainties and their correlations are taken into account.

- A check for a possible left-right bias in the spectrometer acceptance was made by deriving the visible K_S^0 cross section with subsets of the data with opposite signs of decay asymmetry $(p_z^+ - p_z^-)/(p_z^+ + p_z^-)$, where p_z^+ and p_z^- are the components of momentum along the beam direction of π^+ and π^-, respectively). The maximum difference between the values of cross sections for the negative and positive asymmetry samples is 0.7%.

- The fact that the efficiency correction was done on a grid of x_F and p_T bins considerably reduces the dependence of the correction on the shape of the kinematic distributions produced by the MC compared to separate one-dimensional corrections. The remaining uncertainty was studied by varying x_F- and p_T-dependent weighting factors applied to the MC events. The difference between the average efficiency computed with a weight of unity and a weighting map which forces FRITIOF-generated distributions to conform to the corrected data is taken as the systematic uncertainty on the MC production model. The numbers are given in Table 5.

- In [52], we reported evidence for a positive polarization of Λ's relative to the normal to the Λ production plane in the visible region. Nonetheless the acceptance calculations done for the present measurement assume unpolarized production of Λ's. It is however also shown in [53] that the acceptance is insensitive to polarization effects.

- The proper lifetimes of K_S^0, Λ and $\bar{\Lambda}$ extracted from the data sample are $2.65 \pm 0.04\,\mathrm{cm}$, $8.70 \pm 0.47\,\mathrm{cm}$ and $8.26 \pm 0.68\,\mathrm{cm}$, respectively (statistical errors only). The K_S^0 and $\bar{\Lambda}$ lifetimes are within $1\,\sigma$ of the PDG values [38] while the measured Λ lifetime is $1.7\,\sigma$ higher than the PDG value. The level of agreement is thus acceptable.

The systematic uncertainty estimates resulting from these considerations are collected in Table 5. The systematic uncertainties on the differential cross section measurements are quadratic sums of luminosity-dependent and V^0-type dependent terms and are largely correlated over the measured range and constant to within about 20%. Since the uncertainties are for the most part correlated and constant, they appear as uncertainties in the overall scale depending only on target material and V^0 type and are quoted in Tables 6, 7 and 8.

7 Summary

We have studied the production cross sections for K_S^0, Λ, and $\bar{\Lambda}$ in the central region $(-0.12 < x_F < 0.0)$ in proton interactions on nuclear targets (carbon, titanium and tungsten) at a center-of-mass energy of $\sqrt{s} = 41.6\,\mathrm{GeV}$. The main results, the doubly differential cross sections are presented in Tables 6, 7, and 8. Several derived quantities: particle ratios, the A-dependence parameter α, and the total production cross sections are presented and discussed. The results are compared to PYTHIA and EPOS calculations. For the most part, the EPOS calculations agree with the data at the 20% level. PYTHIA is not designed to handle proton nucleus interactions and, as expected, produces p_T distributions which are steeper than the data. PYTHIA also fails to describe the ratio of Λ to $\bar{\Lambda}$, and, as previously pointed out in [26], the ratio of Λ to K_S^0. The failure cannot be attributed to A-dependence. The results are also compared to existing measurements and possible reasons for some discrepancies are discussed.

Acknowledgments

References

[1] N. N. Biswas *et al.*, Nucl. Phys. B **167**, 41 (1980)

[2] S. Mikocki *et al.*, Phys. Rev. D **34**, 42 (1986)

[3] D. Ljung *et al.*, Phys. Rev. **15**, 3163 (1977)

Table 6: The inclusive doubly differential cross section $d^2\sigma_{pA}/dx_F dp_T^2$ for the production of K_S^0 mesons on the indicated targets in the given x_F and p_T bins. The uncertainties given for each bin are statistical. The values marked with asterisks are extrapolated. Additional scale uncertainties (see Sect. 6) are quoted in the headers of each sub-table. The sums over the kinematic bins in each column (row) is given in the last column (row). The corresponding cross section for the column (row) is the sum multiplied by the appropriate bin width.

$d^2\sigma_{pA}/dx_F dp_T^2$, [mb/(GeV/c)²]							
$p + C \rightarrow K_S^0 + X$ (scale uncertainty: ±7.4%)							
$\Delta p_T^2/\Delta x_F$	-0.12 − -0.10	-0.10 − -0.08	-0.08 − -0.06	-0.06 − -0.04	-0.04 − -0.02	-0.02 − 0.0	sum
0.0 − 0.25	219. ± 12.*	352. ± 14.*	715. ± 70.	829. ± 24.	1354. ± 15.	1973. ± 15.	5443. ± 79.
0.25 − 0.5	92.8 ± 3.2*	140.8 ± 3.4*	210. ± 11.	297.6 ± 7.1	425.5 ± 6.6	554.8 ± 7.2	1722. ± 17.
0.5 − 0.75	39. ± 16.	55.5 ± 5.8	92.8 ± 4.6	131.8 ± 4.1	179.7 ± 4.2	207.9 ± 4.4	707. ± 19.
0.75 − 1.0	28.6 ± 5.2	31.3 ± 3.1	49.9 ± 3.2	64.9 ± 2.9	90.6 ± 3.2	99.7 ± 3.2	365.1 ± 8.7
1.0 − 1.25	22.8 ± 5.1	19.8 ± 2.1	25.2 ± 1.9	38.1 ± 2.2	50.0 ± 2.5	60.9 ± 2.9	216.8 ± 7.4
1.25 − 1.5	8.6 ± 2.0	10.9 ± 1.5	16.7 ± 1.7	19.3 ± 1.4	29.3 ± 2.1	31.1 ± 2.1	115.9 ± 4.4
1.5 − 1.75	4.9 ± 1.3	8.9 ± 1.5	11.9 ± 1.6	15.7 ± 1.6	15.7 ± 1.4	19.3 ± 1.7	76.4 ± 3.7
1.75 − 2.0	4.5 ± 1.3	7.8 ± 1.6	9.7 ± 1.6	11.0 ± 1.5	11.2 ± 1.3	9.9 ± 1.1	54.2 ± 3.4
2.0 − 2.25	3.1 ± 0.7	2.8 ± 0.7	6.6 ± 1.3	6.9 ± 1.0	11.5 ± 2.2	8.7 ± 1.3	39.6 ± 3.2
2.25 − 2.5	3.5 ± 0.9	4.6 ± 1.5	4.2 ± 0.9	4.2 ± 0.9	5.0 ± 0.9	5.9 ± 1.1	27.4 ± 2.6
sum	427. ± 21.	635. ± 16.	1143. ± 71.	1418. ± 25.	2173. ± 17.	2971. ± 18.	8767. ± 84.
$p + Ti \rightarrow K_S^0 + X$ (scale uncertainty: ±7.6%)							
$\Delta p_T^2/\Delta x_F$	-0.12 − -0.10	-0.10 − -0.08	-0.08 − -0.06	-0.06 − -0.04	-0.04 − -0.02	-0.02 − 0.0	sum
0.0 − 0.25	936. ± 54.*	1439. ± 63.*	2760. ± 330.	3404. ± 120.	4750. ± 61.	6950. ± 52.	20240 ± 370.
0.25 − 0.5	386. ± 15.*	562. ± 15.*	745. ± 41.	1124. ± 29.	1523. ± 23.	1989. ± 25.	6328. ± 64.
0.5 − 0.75	189.5 ± 5.5*	283. ± 31.	348. ± 19.	471. ± 16.	640. ± 14.	795. ± 16.	2727. ± 45.
0.75 − 1.0	185. ± 38.	157. ± 19.	222. ± 16.	249. ± 11.	324. ± 11.	397. ± 12.	1533. ± 49.
1.0 − 0.25	57. ± 13.	73. ± 11.	119. ± 11.	139.0 ± 8.2	169.3 ± 8.0	212. ± 10.	770. ± 25.
1.25 − 1.5	37.0 ± 8.7	54.2 ± 8.1	69.4 ± 6.9	104.2 ± 8.3	112.4 ± 7.4	127. ± 8.	504. ± 20.
1.5 − 1.75	33.8 ± 8.3	33.4 ± 7.2	48.6 ± 6.6	64.8 ± 6.8	62.3 ± 5.1	71.0 ± 6.1	314. ± 17.
1.75 − 2.0	15.8 ± 5.5	22.6 ± 4.4	33.0 ± 5.2	40.0 ± 4.8	45.0 ± 4.9	51.8 ± 5.8	208. ± 13.
2.0 − 2.25	15.8 ± 5.6	19.3 ± 6.2	22.6 ± 4.4	23.1 ± 3.5	38.2 ± 5.9	30.4 ± 4.4	149. ± 12.
2.25 − 2.5	9.8 ± 4.5	14.3 ± 4.1	12.9 ± 3.4	19.7 ± 3.9	20.8 ± 3.9	27.4 ± 4.8	105. ± 10.
sum	1865. ± 70.	2658. ± 76.	4380. ± 340.	5640. ± 130.	7685. ± 69.	10651. ± 62.	32880. ± 390.
$p + W \rightarrow K_S^0 + X$ (scale uncertainty: ±6.9%)							
$\Delta p_T^2/\Delta x_F$	-0.12 − -0.10	-0.10 − -0.08	-0.08 − -0.06	-0.06 − -0.04	-0.04 − -0.02	-0.02 − 0.0	sum
0.0 − 0.25	3750. ± 180.*	5610. ± 200.*	10940. ± 980.	12420. ± 340.	17460. ± 180.	24040. ± 150.	74220. ± 1100.
0.25 − 0.5	1614. ± 50.*	2284. ± 49.*	2890. ± 130.	4105. ± 87.	5758. ± 71.	7019. ± 72.	23670. ± 200.
0.5 − 0.75	688. ± 205.	879. ± 84.	1409. ± 58.	1985. ± 48.	2441. ± 43.	2862. ± 46.	10270. ± 240.
0.75 − 1.0	478. ± 79.	625. ± 47.	822. ± 39.	1080. ± 35.	1285. ± 33.	1471. ± 36.	5760. ± 120.
1.0 − 0.25	246. ± 40.	289. ± 26.	485. ± 30.	611. ± 27.	729. ± 26.	797. ± 27.	3157. ± 73.
1.25 − 1.5	159. ± 26.	243. ± 25.	310. ± 24.	382. ± 21.	389. ± 19.	458. ± 22.	1940. ± 56.
1.5 − 1.75	142. ± 23.	177. ± 20.	225. ± 22.	287. ± 21.	287. ± 18.	321. ± 20.	1439. ± 50.
1.75 − 2.0	84. ± 16.	113. ± 16.	143. ± 17.	181. ± 17.	196. ± 17.	214. ± 19.	930. ± 42.
2.0 − 2.25	78. ± 15.	82. ± 13.	84. ± 12.	103. ± 12.	111. ± 12.	152. ± 16.	610. ± 33.
2.25 − 2.5	43. ± 11.	59. ± 12.	66. ± 10.	87. ± 13.	87. ± 11.	86. ± 12.	428. ± 28.
sum	7280. ± 300.	10360. ± 240.	17370. ± 990.	21240. ± 360.	28740. ± 200.	37420. ± 180.	122420. ± 1150.

Table 7: The inclusive doubly differential cross section $d^2\sigma_{pA}/dx_F dp_T^2$ for the production of Λ baryons on the indicated targets in the given x_F and p_T bins. The uncertainties given for each bin are statistical. The values marked with asterisks are extrapolated. Additional scale uncertainties (see Sect. 6) are quoted in the headers of each sub-table. The sums over the kinematic bins in each column (row) is given in the last column (row). The corresponding cross section for the column (row) is the sum multiplied by the appropriate bin width.

$d^2\sigma_{pA}/dx_F dp_T^2$, [mb/(GeV/c)²]						
$p + C \to \Lambda + X$ (scale uncertainty: $\pm 8.6\%$)						
$\Delta p_T^2/\Delta x_F$ -0.12 − -0.10	-0.10 − -0.08	-0.08 − -0.06	-0.06 − -0.04	-0.04 − -0.02	-0.02 − 0.0	sum
0.0 − 0.25 123.8 ± 8.5	154.0 ± 8.7	171.7 ± 8.1	192.3 ± 8.4	261. ± 12.	229. ± 22.	1132. ± 30.
0.25 − 0.5 55.4 ± 4.1	62.6 ± 4.0	90.2 ± 4.2	99.0 ± 4.2	125.3 ± 5.0	150.9 ± 7.8	583. ± 12.
0.5 − 0.75 35.3 ± 3.6	47.0 ± 3.6	45.0 ± 3.0	55.7 ± 3.3	60.0 ± 3.2	79.3 ± 4.8	322.3 ± 8.9
0.75 − 1.0 23.6 ± 3.2	27.8 ± 3.2	30.2 ± 2.8	32.1 ± 2.7	41.1 ± 3.1	47.2 ± 3.8	201.9 ± 7.7
1.0 − 0.25 16.7 ± 2.8	15.3 ± 2.2	22.3 ± 3.2	31.2 ± 4.0	26.4 ± 2.8	29.2 ± 3.3	141.1 ± 7.6
1.25 − 1.5 13.8 ± 4.0	10.2 ± 2.2	15.3 ± 3.2	14.5 ± 2.2	14.8 ± 2.2	16.4 ± 2.2	85.0 ± 6.8
1.5 − 1.75 11.4 ± 3.6	10.2 ± 2.4	6.0 ± 1.2	9.5 ± 1.7	13.4 ± 3.2	11.4 ± 2.0	61.9 ± 6.1
1.75 − 2.0 3.7 ± 1.0	5.5 ± 1.8	3.1 ± 0.8	6.1 ± 1.4	6.7 ± 1.4	5.5 ± 1.2	30.7 ± 3.2
2.0 − 2.25 4.3 ± 1.3	5.8 ± 3.1	7.0 ± 4.8	6.0 ± 2.0	3.5 ± 1.0	3.8 ± 1.2	30.3 ± 6.4
2.25 − 2.5 5.9 ± 4.7	2.4 ± 1.0	1.2 ± 0.4	5.9 ± 3.1	2.1 ± 0.6	5.1 ± 1.8	22.7 ± 6.0
sum 294. ± 13.	341. ± 12.	392. ± 12.	452. ± 12.	555. ± 15.	578. ± 24.	2612. ± 38.
$p + Ti \to \Lambda + X$ (scale uncertainty: $\pm 8.7\%$)						
$\Delta p_T^2/\Delta x_F$ -0.12 − -0.10	-0.10 − -0.08	-0.08 − -0.06	-0.06 − -0.04	-0.04 − -0.02	-0.02 − 0.0	sum
0.0 − 0.25 478. ± 32.	533. ± 30.	654. ± 30.	738. ± 30.	837. ± 37.	1181. ± 86.	4420. ± 110.
0.25 − 0.5 243. ± 17.	274. ± 15.	358. ± 16.	395. ± 16.	440. ± 17.	463. ± 23.	2172. ± 43.
0.5 − 0.75 195. ± 21.	166. ± 12.	195. ± 12.	220. ± 12.	268. ± 14.	274. ± 16.	1318. ± 36.
0.75 − 1.0 90. ± 14.	87.4 ± 8.4	113. ± 10.	125. ± 10.	151. ± 10.	193. ± 16.	759. ± 29.
1.0 − 0.25 53. ± 10.	76. ± 11.	82. ± 10.	94. ± 10.	92.7 ± 9.2	105. ± 11.	502. ± 25.
1.25 − 1.5 57. ± 14.	36.8 ± 5.9	43.9 ± 6.7	49.0 ± 6.2	72.1 ± 9.5	70.4 ± 8.8	329. ± 22.
1.5 − 1.75 27.9 ± 7.5	62. ± 23.	27.4 ± 4.8	39.3 ± 6.9	40.6 ± 7.7	63. ± 13.	260. ± 30.
1.75 − 2.0 11.6 ± 3.8	14.9 ± 3.0	34. ± 14.	24.1 ± 4.6	35.7 ± 9.0	27.2 ± 6.0	147. ± 19.
2.0 − 2.25 16.8 ± 8.1	12.0 ± 0.7*	30. ± 14.	14.9 ± 4.3	27.1 ± 7.4	24.7 ± 6.4	126. ± 19.
2.25 − 2.5 5.9 ± 2.9	5.8 ± 2.2	17.7 ± 8.0	7.0 ± 2.0	13.7 ± 5.0	16.2 ± 8.7	66. ± 14.
sum 1177. ± 48.	1268. ± 45.	1555. ± 45.	1705. ± 40.	1977. ± 48.	2417. ± 94.	10100. ± 140.
$p + W \to \Lambda + X$ (scale uncertainty: $\pm 8.2\%$)						
$\Delta p_T^2/\Delta x_F$ -0.12 − -0.10	-0.10 − -0.08	-0.08 − -0.06	-0.06 − -0.04	-0.04 − -0.02	-0.02 − 0.0	sum
0.0 − 0.25 1910. ± 110.	2075. ± 93.	2584. ± 92.	2900. ± 93.	3452. ± 119.	4080. ± 260.	17000. ± 340.
0.25 − 0.5 1053. ± 58.	1194. ± 53.	1260. ± 44.	1517. ± 47.	1708. ± 50.	2012. ± 80.	8740. ± 140.
0.5 − 0.75 641. ± 43.	736. ± 40.	849. ± 40.	820. ± 33.	949. ± 37.	1096. ± 49.	5091. ± 99.
0.75 − 1.0 379. ± 35.	405. ± 33.	482. ± 31.	585. ± 33.	631. ± 32.	687. ± 39.	3168. ± 83.
1.0 − 0.25 276. ± 31.	289. ± 27.	323. ± 28.	387. ± 30.	411. ± 31.	384. ± 27.	2069. ± 71.
1.25 − 1.5 128. ± 20.	190. ± 23.	237. ± 27.	270. ± 31.	302. ± 31.	271. ± 26.	1398. ± 64.
1.5 − 1.75 171. ± 33.	175. ± 30.	199. ± 32.	136. ± 16.	177. ± 23.	180. ± 22.	1038. ± 65.
1.75 − 2.0 94. ± 25.	124. ± 25.	122. ± 21.	136. ± 24.	127. ± 21.	135. ± 23.	739. ± 57.
2.0 − 2.25 42. ± 11.	144. ± 47.	126. ± 40.	131. ± 39.	111. ± 30.	87. ± 17.	640. ± 81.
2.25 − 2.5 38. ± 17.	93. ± 44.	82. ± 30.	70. ± 19.	96. ± 24.	65. ± 15.	443. ± 65.
sum 4730. ± 150.	5430. ± 150.	6270. ± 140.	6950. ± 130.	7960. ± 150.	9000. ± 280.	40330. ± 430.

Table 8: The inclusive doubly differential cross section $d^2\sigma_{pA}/dx_F dp_T^2$ for the production of $\bar{\Lambda}$ baryons on the indicated targets in the given x_F and p_T bins. The uncertainties given for each bin are statistical. The values marked with asterisks are extrapolated. Additional scale uncertainties (see Sect. 6) are quoted in the headers of each sub-table. The sums over the kinematic bins in each column (row) is given in the last column (row). The corresponding cross section for the column (row) is the sum multiplied by the appropriate bin width.

$d^2\sigma_{pA}/dx_F dp_T^2$, $[\mathrm{mb}/(\mathrm{GeV/c})^2]$							
$p + C \rightarrow \bar{\Lambda} + X$ (scale uncertainty: $\pm 10.6\%$)							
$\Delta p_T^2/\Delta x_F$	-0.12 − -0.10	-0.10 − -0.08	-0.08 − -0.06	-0.06 − -0.04	-0.04 − -0.02	-0.02 − 0.0	sum
$0.0 - 0.25$	58.5 ± 9.2	72.6 ± 8.3	83.0 ± 7.0	109.4 ± 7.5	134.7 ± 9.6	$123. \pm 21.$	$581. \pm 28.$
$0.25 - 0.5$	26.2 ± 3.7	31.0 ± 3.2	43.8 ± 3.3	67.2 ± 3.8	68.3 ± 3.7	81.2 ± 5.6	317.7 ± 9.7
$0.5 - 0.75$	15.2 ± 2.6	16.6 ± 2.2	22.6 ± 2.1	32.2 ± 2.6	44.7 ± 2.9	42.3 ± 3.1	173.5 ± 6.4
$0.75 - 1.0$	10.9 ± 1.9	8.7 ± 1.4	16.7 ± 2.4	21.9 ± 2.3	22.7 ± 2.3	21.5 ± 2.3	102.4 ± 5.2
$1.0 - 0.25$	4.5 ± 1.7	7.4 ± 1.4	9.0 ± 1.6	14.0 ± 2.1	12.9 ± 2.1	16.1 ± 1.9	63.7 ± 4.4
$1.25 - 1.5$	6.6 ± 2.2	3.1 ± 0.8	5.7 ± 1.3	5.5 ± 1.1	5.2 ± 1.1	7.8 ± 1.3	33.9 ± 3.4
$1.5 - 1.75$	1.6 ± 0.7	3.2 ± 1.0	5.0 ± 1.6	5.1 ± 1.3	5.9 ± 2.0	5.1 ± 1.1	25.9 ± 3.3
$1.75 - 2.0$	1.4 ± 0.6	2.0 ± 0.8	1.7 ± 0.7	6.3 ± 2.4	3.3 ± 1.3	4.8 ± 1.7	19.5 ± 3.5
$2.0 - 2.25$	0.7 ± 0.5	1.1 ± 0.8	1.7 ± 1.2	4.6 ± 2.1	2.3 ± 0.8	1.3 ± 0.6	11.7 ± 2.8
$2.25 - 2.5$	0.8 ± 0.5	2.7 ± 1.2	0.7 ± 0.4	$1.0 \pm 0.1^*$	1.4 ± 1.0	2.3 ± 1.6	9.0 ± 2.3
sum	$126. \pm 11.$	$148. \pm 10.$	189.9 ± 8.9	$267. \pm 10.$	$301. \pm 12.$	$305. \pm 22.$	$1338. \pm 32.$
$p + Ti \rightarrow \bar{\Lambda} + X$ (scale uncertainty: $\pm 10.7\%$)							
$\Delta p_T^2/\Delta x_F$	-0.12 − -0.10	-0.10 − -0.08	-0.08 − -0.06	-0.06 − -0.04	-0.04 − -0.02	-0.02 − 0.0	sum
$0.0 - 0.25$	$160. \pm 32.$	$190. \pm 29.$	$320. \pm 28.$	$445. \pm 28.$	$513. \pm 35.$	$689. \pm 83.$	$2320.. \pm 110.$
$0.25 - 0.5$	$82. \pm 15.$	$109. \pm 12.$	$151. \pm 11.$	$216. \pm 12.$	$278. \pm 14.$	$358. \pm 22.$	$1193. \pm 37.$
$0.5 - 0.75$	$72. \pm 19.$	$81. \pm 11.$	$119. \pm 12.$	121.0 ± 8.6	$175. \pm 12.$	$182. \pm 14.$	$750. \pm 32.$
$0.75 - 1.0$	25.6 ± 7.2	39.2 ± 7.0	51.1 ± 6.3	73.7 ± 7.7	98.1 ± 9.6	83.0 ± 7.9	$371. \pm 19.$
$1.0 - 0.25$	$56. \pm 31.$	23.8 ± 4.6	39.5 ± 6.6	42.7 ± 6.2	45.1 ± 5.3	$68. \pm 10.$	$274. \pm 34.$
$1.25 - 1.5$	12.5 ± 4.6	$32. \pm 11.$	22.3 ± 4.6	28.9 ± 5.1	30.2 ± 5.9	41.6 ± 7.3	$167. \pm 16.$
$1.5 - 1.75$	14.6 ± 6.9	7.7 ± 2.0	18.1 ± 5.8	14.8 ± 3.4	24.8 ± 5.2	21.9 ± 5.0	$102. \pm 12.$
$1.75 - 2.0$	2.1 ± 1.3	$6.3 \pm 0.5^*$	16.5 ± 6.5	11.2 ± 3.6	$37. \pm 18.$	10.6 ± 3.0	$84. \pm 20.$
$2.0 - 2.25$	3.0 ± 1.6	$4.1 \pm 0.4^*$	8.4 ± 4.1	11.3 ± 3.8	8.7 ± 3.5	21.4 ± 9.9	$57. \pm 12.$
$2.25 - 2.5$	$2.2 \pm 0.3^*$	1.9 ± 0.9	2.4 ± 0.8	4.8 ± 2.1	8.6 ± 3.8	6.2 ± 3.3	26.1 ± 5.6
sum	$431. \pm 52.$	$494. \pm 36.$	$748. \pm 35.$	$968. \pm 35.$	$1219. \pm 45.$	$1481. \pm 89.$	$5340. \pm 130.$
$p + W \rightarrow \bar{\Lambda} + X$ (scale uncertainty: $\pm 10.3\%$)							
$\Delta p_T^2/\Delta x_F$	-0.12 − -0.10	-0.10 − -0.08	-0.08 − -0.06	-0.06 − -0.04	-0.04 − -0.02	-0.02 − 0.0	sum
$0.0 - 0.25$	$850. \pm 100.$	$876. \pm 87.$	$1093. \pm 84.$	$1534. \pm 89.$	$1950. \pm 110.$	$2160. \pm 270.$	$8460. \pm 350.$
$0.25 - 0.5$	$426. \pm 48.$	$425. \pm 37.$	$546. \pm 37.$	$702. \pm 35.$	$920. \pm 40.$	$1122. \pm 61.$	$4140. \pm 110.$
$0.5 - 0.75$	$245. \pm 32.$	$327. \pm 30.$	$331. \pm 25.$	$427. \pm 25.$	$523. \pm 29.$	$593. \pm 34.$	$2446. \pm 72.$
$0.75 - 1.0$	$110. \pm 19.$	$145. \pm 18.$	$222. \pm 23.$	$318. \pm 24.$	$305. \pm 21.$	$338. \pm 26.$	$1438. \pm 54.$
$1.0 - 0.25$	$74. \pm 16.$	$135. \pm 20.$	$121. \pm 14.$	$158. \pm 18.$	$200. \pm 19.$	$193. \pm 19.$	$880. \pm 44.$
$1.25 - 1.5$	$109. \pm 29.$	$76. \pm 15.$	$131. \pm 22.$	$135. \pm 20.$	$115. \pm 15.$	$154. \pm 18.$	$720. \pm 50.$
$1.5 - 1.75$	$47. \pm 15.$	$65. \pm 16.$	$62. \pm 11.$	$57. \pm 10.$	$68. \pm 11.$	$93. \pm 16.$	$391. \pm 33.$
$1.75 - 2.0$	$34. \pm 11.$	$43. \pm 13.$	$50. \pm 13.$	$76. \pm 18.$	$68. \pm 15.$	$53. \pm 12.$	$323. \pm 34.$
$2.0 - 2.25$	$25. \pm 11.$	26.9 ± 8.0	28.4 ± 8.0	$47. \pm 20.$	$54. \pm 15.$	32.4 ± 7.6	$214. \pm 30.$
$2.25 - 2.5$	17.0 ± 6.0	10.4 ± 5.6	20.4 ± 7.4	21.5 ± 7.3	24.0 ± 9.2	$36. \pm 13.$	$129. \pm 21$
sum	$1930. \pm 130.$	$2130. \pm 110.$	$2600. \pm 100.$	$3480. \pm 110.$	$4770. \pm 290.$	$4770. \pm 290.$	$19140. \pm 390.$

[4] D. Bogert *et al.*, Phys. Rev. D **16**, 2098 (1977)

[5] R. T. Edwards *et al.*, Phys.Rev. D **18**, 76 (1978)

[6] B. Y. Oh *et al.*, Nucl. Phys. B **49**, 13 (1972)

[7] V. Blobel *et al.*, Nucl. Phys. B **69**, 454 (1974)

[8] K. Jaeger *et al.*, Phys. Rev. D **11**, 1756 (1975)

[9] H. Bøggild *et al.*, Nucl. Phys. B **57**, 77 (1973)

[10] M. Alston-Garnjost *et al.*, Phys. Rev. Lett. **35**, 142 (1975)

[11] J. W. Chapman *et al.*, Phys. Lett. B **47**, 465 (1973)

[12] K. Jaeger *et al.*, Phys. Rev. D **11**, 2405 (1975)

[13] A. Sheng *et al.*, Phys. Rev. D **11**, 1733 (1975)

[14] K. Heller *et al.*, Phys. Rev. D **16**, 2737 (1977)

[15] P. Skubic *et al.*, Phys. Rev. D **18**, 3115 (1978)

[16] F. T. Dao *et al.*, Phys. Rev. Lett. **30**, 1151 (1973)

[17] M. Asai *et al.*, Z. Phys. **C27**, 11 (1985)

[18] H. Kichimi *et al.*, Phys. Rev. D **20**, 37 (1979)

[19] A. Aleev *et al.*, Yad. Fiz. **44** 661, (1986); Sov. J. Nucl. Phys. **44**(3) 429, (1986)

[20] M. I. Adamovich *et al.*, Eur. J. Phys. C **26**, 357 (2003)

[21] F. W. Büsser *et al.*, Phys. Lett. B **61**, 309 (1976)

[22] S. Erhan *et al.*, Phys. Lett. B **85**, 447 (1979)

[23] D. Drijard *et al.*, Z. Phys. C **9**, 293 (1981)

[24] D. Drijard *et al.*, Z. Phys. C **12**, 217 (1982)

[25] G. Bocquet et al., Phys. Lett. B **366**, 441 (1996)

[26] B.I. Adelev et al., Phys. Rev. C **75**, 064901 (2007)

[27] H. Jiang and X. Cai, Acta Phys. Hung. A **25**, 313 (2006)

[28] T. Sjostrand et al., Comp. Phys. Commun. **135**, 238 (2001)

[29] K. Werner et al., Phys. Rev. C **74**, 044902 (2006)

[30] I. Abt et al., Eur.Phys.J. C **29**, 181 (2003)

[31] E Hartouni. et al., HERA-B Design Report, DESY-PRC **95/01**, (1995)

[32] K. Ehret et al., Nucl Instr. Meth. A **446**, 190 (2000)

[33] C. Bauer et al., Nucl. Instr. Meth. A **501**, 39 (2003)

[34] H. Albrecht et al., Nucl. Instr. Meth. A **555**, 319 (2005); H. Albrecht et al., Nucl. Instr. Meth. A **541**, 610 (2005)

[35] I. Ariño et al., Nucl. Instr. Meth. A **516**, 445 (2004)

[36] G. Avoni et al., Nucl. Instr. Meth A **580**, 1209 (2007)

[37] V. Eiges et al., Nucl. Instr. Meth A **461**, 104 (2001)

[38] C. Amsler et al., Phys. Lett. B **667**, 1 (2008)

[39] I. Abt et al., Nucl. Instr. Meth. A **582**, 401 (2007)

[40] I. Abt et al., Nucl. Instr. Meth. A **490**, 546 (2002)

[41] J. Podolansky and R. Armenteros, Fhil. Mag. **45**, 13 (1954)

[42] H. Pi, Comp. Phys. Comm. **71**, 173 (1992)

[43] R. Brun et al., GEANT3, CERN-DD-EE-84-1 (1987)

[44] S. Brodsky and J. Gunion, Phys. Rev. D **17**, 848, (1978)

[45] G.W. van Apeldoorn et al., Nucl. Phys. B **91**, 1 (1975)

[46] M. Bardadin-Otwinowska et al., Phys Lett **21**, 351 (1966)

[47] J. Cronin et al., Phys. Rev. Lett. **38**, 670 (1977)

[48] W.M. Geist, Nucl. Phys. A **525**, 149 (1991)

[49] R. Pernack, PhD thesis, University of Rostock (2004)

[50] HEPData DB, Durham, http://durpdg.dur.ac.uk/cgi-hepdata/hepreac/851590.

[51] S. Erhan, Priv. Comm.

[52] I. Abt et al., Phys. Lett. B **638**, 415, 2006

[53] E. Klinkby, Masters thesis, University of Copenhagen (2004).